PNAS RESEARCH ARTICLE | APPLIED PHYSICAL SCIENCES

Chiral structural color from microdomes

Xintao Lai[a,b,1], Tongyu Li[c,1,2], Xiaoyu Hou[b,1], Florian Vogelbacher[d], Jiajun Wang[c], Yanlin Song[b], Lei Shi[c,e,3], and Mingzhu Li[a,f,3]

Affiliations are included on p. 8.

Edited by David Weitz, Harvard University, Cambridge, MA; received September 18, 2024; accepted January 21, 2025

Artificial chiral-structural-color materials can carry high-dimensional information based on multiple optical degrees of freedom, providing possibilities for advanced optical security and information storage. However, current artificial chiral-structural-color materials are hindered by their specific compositions, fine nanostructures, and single polarization modulation. Here, we found that microdomes made from common polymers have chiral structural colors with broadband tunability and multiple polarization-modulated chirality. The microdome patterns are easily fabricated by ordinary printing techniques and have inhomogeneous spatial distributions of full polarization states and customizable colors. Our chiral-structural-color microdomes (CSCMs) provide a promising roadmap for high-capacity information encryption and high-security anti-counterfeiting. We developed multidimensional tunable structural color displays and achieved encryption with high information capacity. To further highlight the application potential, we constructed contact lenses integrated with CSCMs for identity authentication with 2^{32} distinctive cryptograms.

chirality | structural color | encryption | anti-counterfeiting

Significance

Chiral-structural-color materials with high-dimensional controllable channels, such as wavelength, amplitude, polarization, and phase, are the excellent candidates for high-capacity information storage and encryption. Currently, most of the artificial chiral-structural-color materials are restricted to specific compositions and sophisticated nanostructures. Meanwhile, they usually exhibit single-handedness, limiting their capacity to control multiple polarization states of light. In this study, we found the tunability and multiple polarization-modulated chirality of the structural colors generated by microdomes made from common polymers, which provides a promising roadmap for high-capacity information encryption and high-security anti-counterfeiting.

Structural color materials, particularly polymer-based structural colors materials (1–3), are sustainable, low cost, nonfading, and responsive to stimuli (4, 5), which has stimulated much interest in different scientific and technological fields ranging from displays (6, 7), sensors (8), and data security (9) to photoelectric devices (10). Among these materials, chiral-structural-color materials have multiple controllable channels, including wavelength, amplitude, polarization, and phase, and are promising candidates for high-capacity information storage and encryption (11–13). In nature, chiral-structural-color materials exist in many organisms (14–16), such as *Chrysina gloriosa* (17), *Pollia condensate* (18), and *Odontodactylus cultrifer* (19), and perform excellent functions for animals and plants (20, 21), including mating, recognizability, warning, and disguise. Inspired by natural organisms, scientists have developed many artificial chiral-structural-color materials with enhanced chiroptical activity (22, 23) and dynamic chirality (24–26), such as chiral molecule-modified photonic crystals (27), helicoidally organized nanoblocks (28, 29), chiral liquid crystallines (30, 31), and chiral metamaterials (32–34). However, most of these artificial chiral-structural-color materials are restricted to specific compositions and sophisticated nanostructures (35, 36). Meanwhile, current artificial chiral-structural-color materials usually exhibit single-handedness (37, 38), limiting their capacity to control multiple polarization states of light for three-dimensional stereo imaging and high-security optical encryption. It remains a great challenge to develop facile chiral-structural-color materials with full-polarization manipulation capability.

Here, we found that the color of microdomes made from common polymers [named as chiral-structural-color microdomes (CSCMs)] has polarization-modulated chirality with the record high dissymmetry factor of ~1.998. We demonstrate experimentally and theoretically that the chiroptical response of CSCMs is due to a phase delay of two orthogonal linearly polarized (LP) components of the LP incident light through multiple total internal reflections (TIRs). The color and the pattern of CSCMs can be easily and precisely regulated by the digital printing method (39, 40). Furthermore, CSCMs have multiple polarization states, and the chiroptical response of CSCMs is broadband tunable and switchable through modulation of the incident polarization. By harnessing these unique optical properties of CSCMs, we realized full-color imaging, high-capacity multichannel information encryption, and high-level identity security. To further demonstrate the application potential of CSCMs, we constructed a contact lens integrated with CSCMs that provides 2^{32} distinctive cryptograms for personal identity proofing. Our work provides a facile and economical strategy for constructing chiral-structural-color materials with multiple degrees of freedom which can provide high information capacity for optical communication, optical anti-counterfeiting, and high-dimensional encryption.

Author contributions: M.L. designed research; X.L., T.L., X.H., F.V., J.W., and M.L. performed research; X.L., T.L., X.H., F.V., J.W., L.S., and M.L. analyzed data; and X.L., T.L., X.H., Y.S., L.S., and M.L. wrote the paper.

The authors declare no competing interest.

This article is a PNAS Direct Submission.

Copyright © 2025 the Author(s). Published by PNAS. This article is distributed under Creative Commons Attribution-NonCommercial-NoDerivatives License 4.0 (CC BY-NC-ND).

[1]X.L., T.L., and X.H. contributed equally to this work.

[2]Present address: Department of Electrical and Computer Engineering, Boston University, Boston, MA 02215.

[3]To whom correspondence may be addressed. Email: lshi@fudan.edu.cn or mingzhu@mail.ipc.ac.cn.

This article contains supporting information online at https://www.pnas.org/lookup/suppl/doi:10.1073/pnas.2419113122/-/DCSupplemental.

Published February 25, 2025.

Downloaded from https://www.pnas.org by FUDAN UNIVERSITY on February 25, 2025 from IP address 202.120.234.33.

Optical Characterization of the CSCMs

We printed a colorful painting "The Starry Night", composed of CSCMs on a hydrophobic polydimethylsiloxane (PDMS) substrate (Fig. 1 *A*–*D*). The hydrophobic PDMS substrate is modified with 1H,1H,2H,2H-perfluorodecyltrimethoxysilane and has a contact angle of 85° with the polymer ink (InkOrmo) (see details in *Methods* and *SI Appendix*, Fig. S1). Thus, the hydrophobic substrate ensures large curvature angles (CAs) of the microdomes to achieve a high-saturation color for the CSCMs (*SI Appendix*, Figs. S2 and S3), due to the increase of the TIR trajectories. These CSCMs show size-dependent coloration (Fig. 1 *B* and *C* and *SI Appendix*, Figs. S4 and S5) because different sizes of the microdomes can lead to varying trajectories of TIR and interference paths (40).

Besides the vivid structural color, we found that the CSCMs exhibit polarization-dependent chiroptical responses throughout the visible regime (Fig. 1*D* and *SI Appendix*, Figs. S6 and S7). As shown in Fig. 1*D*, the colorful painting shows distinct optical appearances through the right-hand circular (RHC) polarizer (top row) and the left-hand circular (LHC) polarizer (bottom row) at ψ = 0° or 90° (where ψ represents the polarization angle relative to the y-axis). The result suggests intense chiroptical responses in the CSCMs. Moreover, the brightness of the painting strongly depends on the incident polarization angle (ψ) under an RHC polarizer (or LHC polarizer). When ψ rotates from 0° to 90° with a step of 30°, a smooth and continuous brightness transition of the painting is observed, indicating the switchable chirality of the CSCMs.

We theoretically predict that such a fascinating switchable chirality of the CSCM originates from the inhomogeneous spatial distribution of the polarization state of the scattered light (Fig. 1*E*). We used closed-packed microsphere (~10 μm in diameter) as template and fabricated a hexagonal close-packed microdomes (~4.9 μm radius) film over a large area (10 cm × 10 cm) (Fig. 1*F* and *SI Appendix*, Figs. S8–S10) for circular dichroism (CD) spectroscopy detection (Fig. 1*F* and *SI Appendix*, Fig. S11). The closely packed microdome arrays have a high density of structures, which enhances the reflection of light, leading to the superior optical performance. The film shows bright green color and presents very strong CD peaks (a maximum CD intensity of ~400 mdeg) in the visible region. Notably, the peak position of the CD response well matches the reflection peak position of the CSCM (*SI Appendix*, Fig. S12). We recorded the intensity of the CD signals at the wavelength of 650 nm under different α (α is the azimuthal angle, defined as the angle with respect to the incident polarization direction) (Fig. 1*G*). The CD signals at different α are obtained by applying in-plane rotation of the film. Distinctively, the sign of the CD peaks is switched between negative and positive by changing α. There are four transitions in CD value from negative to positive (or from positive to negative) as α increases, demonstrating that the opposite circular polarization distributes at two orthogonal azimuthal angles. The results identify the switch ability of the chiral structural color of the CSCMs. Moreover, we calculated the maximum dissymmetry factor, $g = 2(I_l - I_r)/(I_l + I_r)$, which get the record high ~1.998 (*SI Appendix*, Table S1). Such an attractive chiroptical response indicates that the microdome structure is an architecture that generates structural color and gives rise to chirality.

Mechanism of the Chirality

The CSCM chirality originates from different phase shifts of the s-polarized and p-polarized components of LP incident light in TIRs,

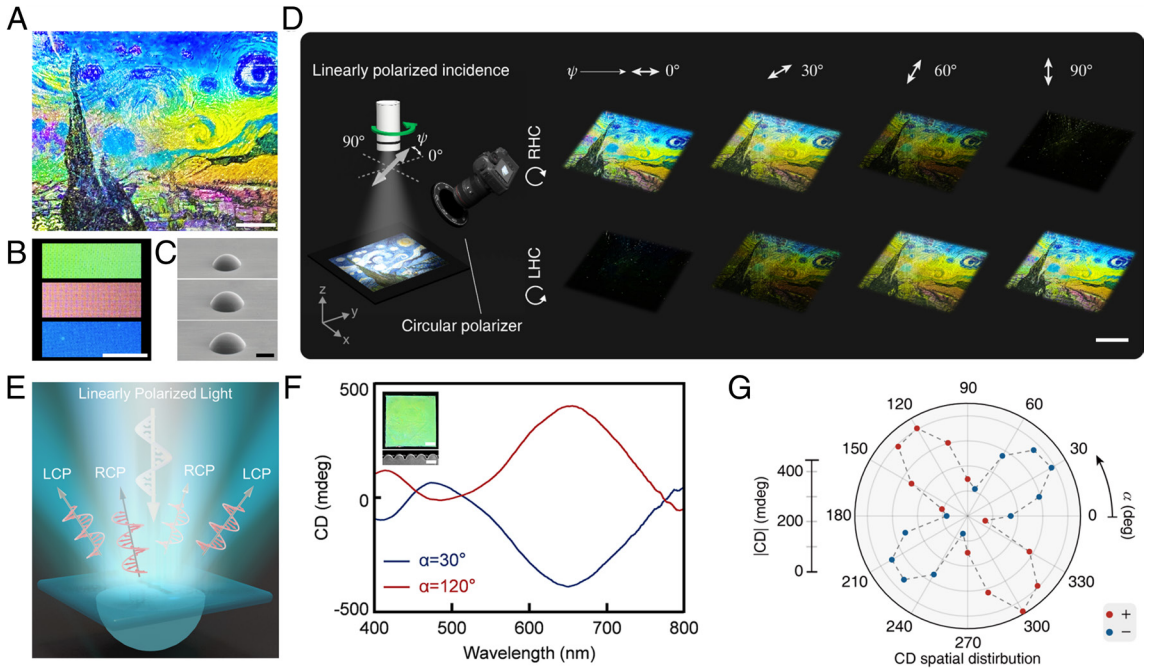

Fig. 1. Optical properties of the CSCMs. (*A*) The reconstruction image of the masterpiece of Vincent van Gogh's The Starry Night. The reconstruction image is fabricated by the inkjet-printing method and contains CSCMs with different radiuses. (Scale bar, 5 mm.) (*B*) The printed multicolor panels composed of red, green, and blue palettes. These palettes are used to print the painting The Starry Night. (Scale bar, 5 mm.) (*C*) Scanning electron microscopy (SEM) micrographs of the printed CSCM pixels with different radiuses, corresponding to (*B*). (Scale bar, 10 μm.) (*D*) The image The Starry Night was viewed through an RHC polarizer (first line) and an LHC polarizer (second line) at different incident polarization angles ψ of 0°, 30°, 60°, and 90°. The brightness of the image changes gradually through the polarized analyzer. (*E*) Schematic of the multiple optical properties of the CSCM. Illuminating by the LP incident white light, the microdome not only shows vivid structural color but also generates chirality. The right-handed circularly polarized (RCP) light and left-handed circularly polarized (LCP) light are distributed in the orthogonal azimuthal direction. (*F*) CD spectra of the close-packed CSCM arrays. The negative and positive CD peaks are measured at different azimuthal angles: α = 30° and α = 120°, respectively. *Inset*: Optical image and scanning electron microscope image of large-scale CSCMs. The optical image shows the bright and uniform structural color of the CSCMs. (Scale bar, 2 cm and 10 μm, respectively.) (*G*) Azimuth angular diagram of the CD spatial distribution of the CSCM at the wavelength of 650 nm with different α. This diagram allows us to visualize all of the CD values for all azimuthal angles in a single image. In addition, the linear dichroism (LD) spectra of the microdome are also recorded to exclude possible LD artifacts.

Downloaded from https://www.pnas.org by FUDAN UNIVERSITY on February 25, 2025 from IP address 202.120.234.33.

as illustrated in Fig. 2*A*. When an LP light normally impinges upon the microdome from the flat side, the TIR will occur on those light rays while $\theta > \arcsin(1/n_1)$ is satisfied (*SI Appendix*, Fig. S14) (41), where θ is the incident angle at the contact surface and n_1 is the refractive index of the microdome. An incident plane can be defined by an incident ray and the normal of its impinged point, on which the polarized direction of the incident ray is sequentially determined. In the TIR process, the energies of the s-polarized and p-polarized components are conserved, but their phase shifts are different, which causes a phase delay $\Delta\varphi(\Delta\varphi = \varphi_s - \varphi_p)$, where φ_s and φ_p are the phase of s- and p-polarization, respectively, more details can be found in *SI Appendix*, Fig. S15) (42). When the accumulated phase delay between two LP bases reaches $\pi/2$, the outcoming light along the $\alpha = \pm 45°$ direction becomes circularly polarized. The chirality depends on the sign of the angle between the incident electric vector and its incident plane.

To further visualize the far-field distribution of the polarization states of CSCMs, we simulated the polarization map of the microdome in the far-field, under the normal incidence of horizontal LP light at 650 nm (Fig. 2*B*) (43). The electric fields are projected into the *x*–*y* plane to define their polarization, corresponding to the paraxial measurement (see details in *Methods*). The phase delays from the experiment and simulation are plotted in Fig. 2*C* and *SI Appendix*, Fig. S16, respectively. These results show an approximately uniform distribution of $\pi/2$ (More detailed discussion of these results can be found in *SI Appendix, Supplementary Text*). Since the s/p-polarized component vanishes at $\alpha = 0°/90°$, making the phase ill-defined, the phase delays along these directions have a low signal-to-noise ratio. These results indicated that the fascinating switchable chirality of the CSCMs originates from the inhomogeneous spatial distribution of the polarization state of the scattered light. Moreover, the distribution of the polarization state can shift linearly with the illumination direction, offering an additional degree of freedom to control the chiral structural color. A detailed discussion of these results can be found in *SI Appendix, Supplementary Text*.

We further performed numerical simulations of the chirality distribution of a single microdome at a wavelength of 650 nm employing the finite-difference time-domain method (Fig. 2*D*, top row and *SI Appendix*, Fig. S23). The far-field numerical simulation results of the microdome show a characteristic interference pattern of concentric rings (i.e., a multiorder diffraction ring) without using polarized analyzers. Furthermore, the characteristic interference pattern transforms into three different broken concentric ring patterns when the scattered light is filtered through the LHC polarizer, RHC polarizer, and LP polarizer, respectively. According to these broken concentric ring patterns, we obtained the distributions of LCP light, RCP light, and LP light. The LCP, RCP, and LP scattered light are distributed in different azimuthal directions, indicating the inhomogeneous spatial distribution of polarization states. To verify the above simulation results, we used a homemade experimental setup to measure the far-field diffraction patterns of the CSCMs with different polarized analyzers (Fig. 2*D*, bottom row and *SI Appendix*, Figs. S24 and S25). A

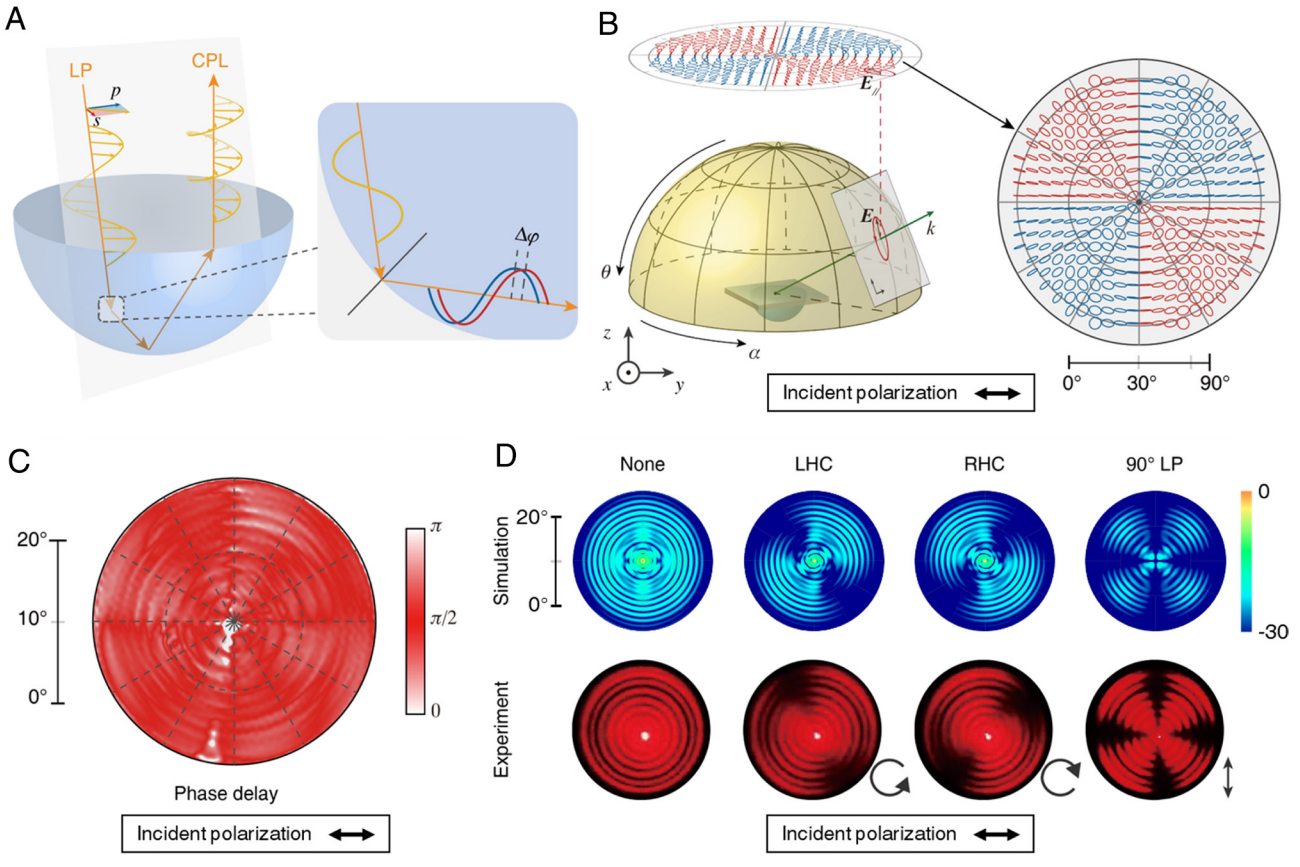

Fig. 2. Mechanism of the chiral phenomenon. (*A*) Schematic diagram of the mechanism of polarization conversion. The s-polarized and p-polarized components gain different phases during the TIR in the incident plane. When the accumulated phase delay after multiple TIRs reaches $\pi/2$, the outcoming LP light becomes circularly polarized. (*B*) The measured polarization map of the CSCMs in the far field under the normal incidence of horizontal LP light at 650 nm. To define the polarization, the electric vectors of the scattering light are projected into the *x*–*y* plane. The RCP light and LCP light are distributed in the orthogonal azimuthal direction. (*C*) The measured map of phase delay between the s-polarized and p-polarized components of the scattering field in the far-field. (*D*) Numerically simulated far-field patterns and the experimental results of the CSCMs at 650 nm wavelength filtered by different polarized analyzers with horizontal polarization incidence.

Downloaded from https://www.pnas.org by FUDAN UNIVERSITY on February 25, 2025 from IP address 202.120.234.33.

collimated LP laser beam illuminates the CSCMs, and a digital camera collects the diffraction light from CSCMs. The experimental results are consistent with the numerical simulation results.

Brightness Control of the CSCM Color

The inhomogeneous distribution of the polarization states of CSCMs depends on the incident polarization angle (ψ). When an LP light with different polarization angles illuminates the CSCMs, the distribution of polarization states rotates according to ψ (*SI Appendix*, Fig. S26). In other words, the intensity of the LCP component scattered from CSCMs changes when we observe CSCMs at a specific direction. In this case, the brightness of the structural color can be readily regulated after being filtered by an RHC polarizer. We built an experimental setup (Fig. 3*A*) to systematically analyze the brightness variations of the structural color scattered from the CSCMs with different incident polarization angles. As Fig. 3*B* shows, the brightness of the prepared CSCMs in cyan is regulated continuously by changing ψ from 0° to 90°. As retrieved from the reflectance spectra (Fig. 3*C*), the peak positions remain identical, but the intensities decrease. These results demonstrate that the brightness of structural color is continuously regulated. We further investigated the relationship between brightness of structural color and the polarization angle (ψ) through experiments and numerical simulations. Our results reveal that the variation of brightness with ψ conforms to a cosine-squared function, analogous to Malus' law. Specifically, the brightness of the structural color can be accurately predicted by the following

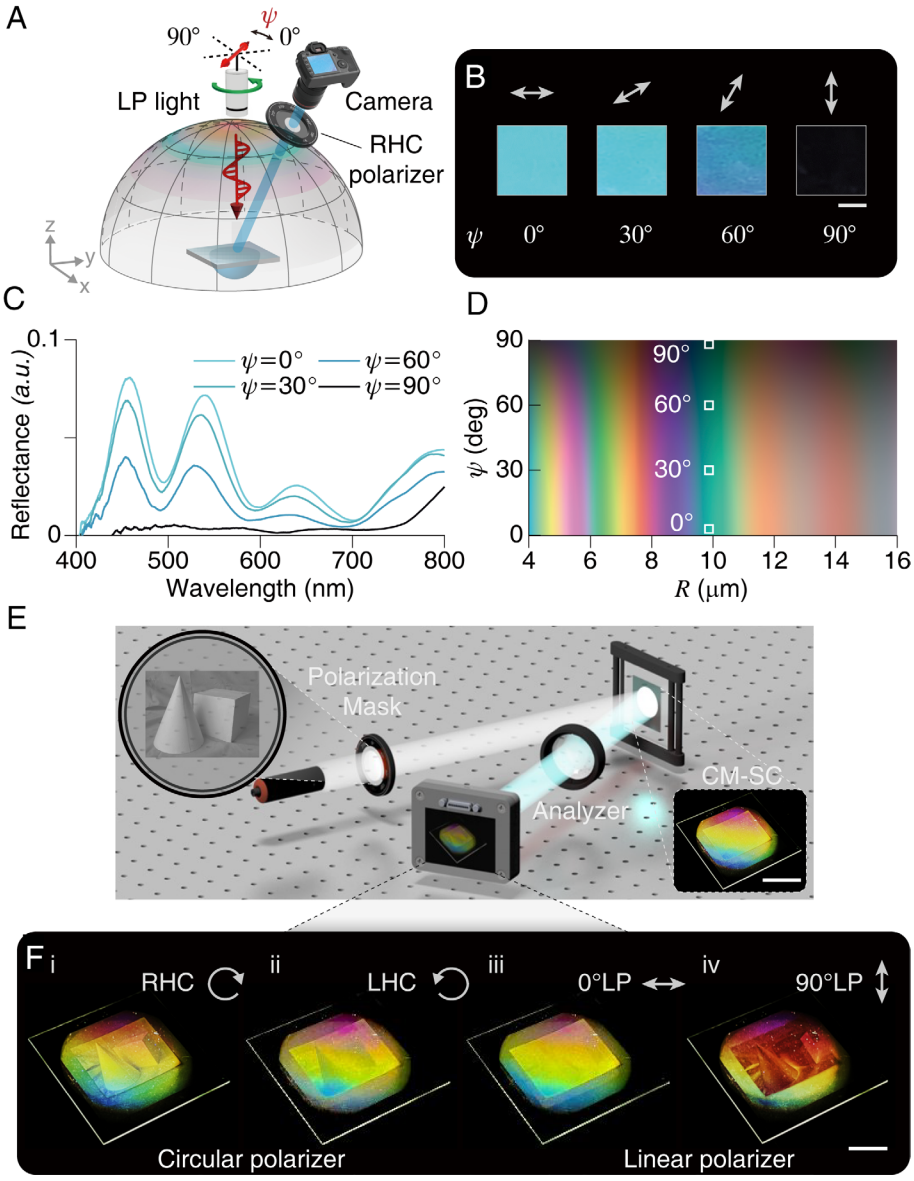

Fig. 3. Brightness tunability of the CSCMs. (*A*) Schematic of the experimental setup used to observe the polarization-dependent structural color scattered from the CSCMs. Collimated white light was used to illuminate the CSCMs. The linear polarizer in an optic mount was placed before the light source to control the polarization angle ψ. The scattered light in a certain azimuth was filtered by an RHC polarizer and then recorded using a camera. (*B*) The brightness regulation of the structural color via changing the polarization angle ψ from 0° to 90°. (Scale bar, 4 mm.) (*C*) The reflectance spectra of the structural color with different brightness in (*B*). (*D*) The simulation results of the structural color regulated by the radius (*R*) and the polarization angle (ψ). The default parameters used in this simulation were CA = 85°, refractive index = 1.54, incident angle = 0°, and received angle = 30°. (*E*) Schematic illustration of the full-color imaging system. The polarization mask is made of a commercially customized patterned liquid crystal polymer polarizer. The polarization pattern in the mask cannot be recognized as the mask is entirely transparent. We can only see an iridescence film with uniform brightness without the analyzer. (Scale bar, 10 mm.) (*F*) Experimental reconstructed images of the sketch reproduced on the 4 cm × 4 cm iridescence pattern with different polarized analyzers (RHC polarizer, LHC polarizer, 0° LP polarizer, and 90° LP polarizer). (Scale bar, 10 mm.)

Downloaded from https://www.pnas.org by FUDAN UNIVERSITY on February 25, 2025 from IP address 202.120.234.33.

formula: $I = I_0\cos^2(\psi + A) + B$, where I_0 is the transmitted light intensity after passing through the first polarizer, I is the intensity of the polarized light after passing the RHC polarizer, ψ is the polarization angle, A and B are constants (A detailed discussion of these results can be found in *SI Appendix*, *Supplementary Text*). In addition, the color of each microdome can be tuned by adjusting its radius which has been demonstrated in our previous work (40). Therefore, the brightness control demonstrated for a single color in this experiment can be readily extended to full-color brightness control (*SI Appendix*, Figs. S28 and S29). We can arbitrarily specify the coloration state (after filtration by the RHC polarizer) of the CSCMs with different R (microdome radius) and ψ (incident polarization angle) through numerical calculations, as shown in Fig. 3*D*. For instance, when the radius of the CSCM is 10.1 μm as same as the sample in Fig. 3*B*, the calculated color is cyan and its brightness changes continuously with ψ from 0° to 90°, which is consistent with our experimental results. Collectively, we can easily obtain any color on demand in the hue, saturation, and value (HSV) color space by optimizing the CSCM radius and the incident polarization angle (*SI Appendix*, Fig. S30).

Controlling the color brightness provides a promising manipulation degree of freedom for carrying information beyond the two-dimensional (2D) HS plane. For example, an image with a shadow rending effect can depict spatial positions of materials and record an object's shade features, which plays a vital role in stereo imaging, machine vision systems, etc. As shown in Fig. 3 *E* and *F*, we created a sketch on CSCMs to achieve full color image with a shadow rending effect. The target sketch and the experimental setup are shown in *SI Appendix*, Figs. S31*A* and S32. The gray level of each pixel in the target sketch represents the designed incidence polarization angle for each CSCM. In the experiment, we fabricated a CSCM pattern of 4 cm × 4 cm (the pattern contains 664 pixels × 664 pixels and each CSCM radius is 8.3 μm) by inkjet printing (Fig. 3 *E*, *Right*). Then, we encoded the target sketch in the polarization profile of light by using a commercially patterned polarization mask. Notably, the polarization pattern in the mask cannot be recognized as the mask is entirely transparent (*SI Appendix*, Fig. S33). Light traveling through the polarization mask is segmented into many regions with different polarization angles (ψ), according to the designed polarization pattern. These different ψ change the spatial distribution of the polarization states of the scattered light from CSCMs, and then affect the color brightness. Consequently, the appearance of the CSCMs is easily altered by applying this patterned polarized light and different polarized analyzers to the optical path (Fig. 3*F*). In Fig. 3 *F*, *i*, we observed an iridescent sketch through an RHC polarizer. The cone and the cube in the sketch are recognizable and show great contrast of light and shadow, providing depth perception. When viewed through the LHC polarizer (Fig. 3 *F*, *ii*), the iridescent sketch exhibited an inverted brightness compared with that in Fig. 3 *F*, *i*. For example, the brightness of the left part of the cone transitions from light to dark. Such an exotic image results from the orthogonality of the RCP and LCP components. In addition, we obtained two different images through two orthogonal LP polarizers (horizontal and vertical polarization) (Fig. 3 *F*, *iii* and *iv*). One image shows almost uniform brightness (Fig. 3 *F*, *iii*), resulting in less detailed levels of the sketch. Thus, the outline of the cone and the cube in the sketch cannot be distinguished. The other exhibits a sketch with low brightness (Fig. 3 *F*, *iv*), but the cone and the cube in the sketch are recognizable. The reason is that the scattered light contains many elliptical polarizations (synthesized by different intensities of the RCP and LCP components) whose long axis is almost parallel to the horizontal direction. Thus, the scattered light can pass through the horizontal LP polarizer. In contrast, it is blocked by the vertical LP polarizer, resulting in light extinction (Fig. 3 *F*, *iv*). These results indicate that several polarization states can serve as independent data-carrying channels.

Multichannel Information Encryption

As the hue and brightness of the CSCM color are sensitive to its morphology and the incident polarization, these color dimensions can be used to encode different messages by designing the arrangement of CSCMs and the polarization angle of incident light (Fig. 4 and *SI Appendix*, Fig. S34). Thus, our CSCMs provide a facile and flexible design with multiple degrees of freedom for high-dimensional optical encryption and decryption. The CSCMs can modulate various characteristics of light including wavelength, amplitude, phase, and polarization for encryption. All these parameters collectively establish a vast key space, enabling optical encryption systems with high security. As a proof of concept, we constructed an image with multichannel information encryption (Fig. 4 *A*, *i*). We first printed the CSCMs portraits (lock) containing both pixels of Mo Zi and Fresnel portraits (500 pixels × 500 pixels). The CSCMs are around 8 μm in radius. As shown in Fig. 4*B*, the two portraits interfere with each other, and the images are difficult to identify under natural light. Then, we designed the patterned linear polarizer (key 1) to control the polarization angle of the incident light pixel-by-pixel. The Mo Zi and Fresnel portraits are encoded onto the polarization profile with polarization angles of 45° and 135°, respectively, and their overlapped pixels are encoded onto the polarization profile with a polarization angle of 90°, as shown in Fig. 4 *A*, *ii* and *SI Appendix*, Fig. S35. The patterned linear polarizer (key 1) is transparent and no image can be observed under normal incident light (Fig. 4*C*). When the light irradiates through the patterned linear polarizer (key 1) onto CSCMs portraits (lock), we obtain LCP, RCP, and LP light, respectively, at a specific viewing angle. After filtering by the LHC polarizer (key 2) and the RHC polarizer (key 2), we get the "Mo Zi" and "Augustin-Jean Fresnel" images in the LCP and RCP channels (Fig. 4*D*), respectively. In summary, our proposed CSCMs provide multilevel protection for information security. First, it allows for the physical splitting of the encrypted information (a lock and two keys). The pattern on the CSCMs can only be visible with both patterned linear polarizer (key 1) and an analyzer (key 2). Second, it requires correct pixel matching between key and lock. Misalignment will lead to incorrect image information. Therefore, the CSCMs meet the requirements for high security and substantial data capacity, making them promising candidates for identity authentication, secure communication, and data storage.

Identity Authentication

To further highlight the application potential of encryption based on CSCMs, we printed a concentric-arc pattern using CSCMs on a contact lens for identity authentication mimicking the personal identification system based on iris patterns (Fig. 5). This CSCM arc pattern successfully implements fivefold encryption functions: number, morphology, orientation, color, and polarization (Fig. 5 *A* and *B*). Among them, "number" represents the quantity of arcs (i), where each arc has a distinct radius, denoted as r_i (*SI Appendix*, Fig. S36). "Morphology" is defined as the arc length l ($l = \alpha_{arc} \cdot r_i$, where α_{arc} is the central angle of the arc) (*SI Appendix*, Fig. S36). "Orientation" describes each arc angular position relative to its center points, defined by the start angle (θ_1) and the ending angle (θ_2) ($\alpha_{arc} = \theta_2 - \theta_1$) (*SI Appendix*, Fig. S36). "Color" refers to the coloration of the arc. Additionally, the chirality of CSCMs is sensitive to the incident polarization. When

Downloaded from https://www.pnas.org by FUDAN UNIVERSITY on February 25, 2025 from IP address 202.120.234.33.

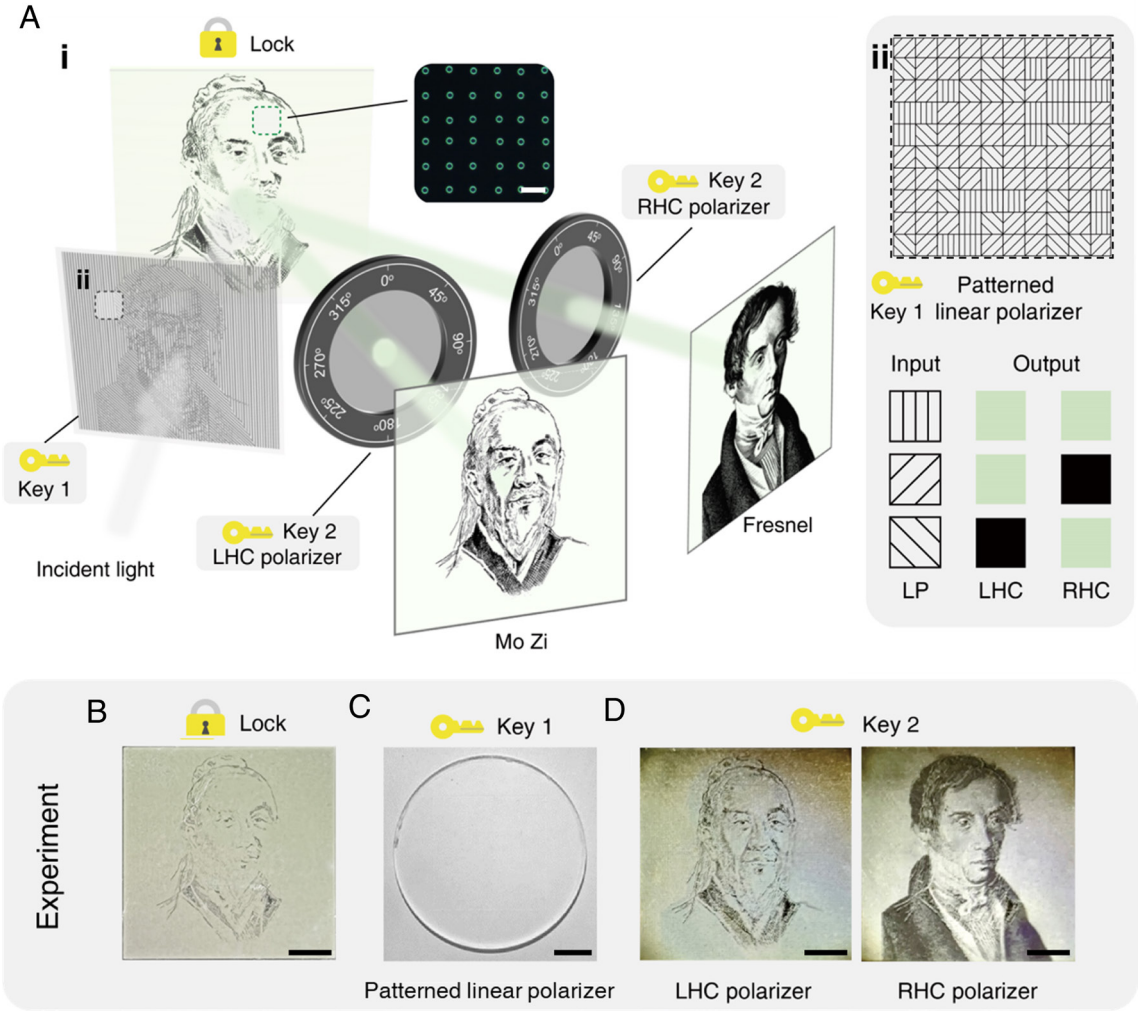

Fig. 4. Applications of the CSCMs. (*A*) Conceptual illustration of the multichannel information encryption via the CSCMs. By elaborate design, the pre-encrypted information is divided into three parts: these are imposed on the CSCMs (lock), the patterned linear polarizer (key 1), and the analyzers (key 2), respectively. The patterned linear polarizer can modulate the incident light. When the light illuminates the cascaded configuration (lock and key 1), it generates two completely different portraits (Mo Zi and Augustin-Jean Fresnel) after being filtered by the LHC polarizer and the RHC polarizer (key 2), respectively. The black dotted line frame shows different unit alignments of the patterned linear polarizer, which determines the polarization states of the scattered light and the principle of encryption. The green dotted line frame shows a selected area from the CSCMs with 6 × 6 pixels. (Scale bar, 60 μm.) (*B* and *C*) Images of the lock and key 1 used in this experiment. (Scale bars, 6 mm and 10 mm, respectively.) (*D*) Experimental results of two portrait images displayed under different viewing modes (LHC polarizer, and RHC polarizer). (Scale bar, 6 mm.) Irrelevant information is filtered out by different polarized analyzers, so the image has no crosstalk.

the incident polarization angle (ψ) is 0°, 45°, 90°, and 135°, CSCMs can generate four different polarization lights, 0°-LP, LCP, 90°-LP, and RCP, respectively. Thus, the combination of number, morphology, orientation, color, and polarization establishes a vast code space due to the orthogonality of these attributes (coding capacity = f(*number, morphology, orientation*, *color*, *polarization*)). For example, we design a pattern with four arcs (*SI Appendix*, Fig. S37), where each arc's α_{arc} equals 90°, 180°, 270°, or 350°; start angles (θ_1) are 0°, 90°, 180°, or 270°; colors are yellow, red, green, or blue; thus, the resulting coding capacity is 2^{24} ($4^4 \times 4^4 \times 4^4$). When the incident light is subdivided into four fan-shaped regions, with the polarization angle (ψ) in each region having four possible orientations (0°, 45°, 90°, or 135°), it allows for the creation of 4^4 distinct polarization profiles. In sum, the resulting coding capacity of the four arcs increases to 2^{32}. The encryption design incorporates polarization variations to introduce a visual dimension and enhances complexity within encryption technology for rigorous personal identification.

Fig. 5*C* shows the top-view (convex side of the contact lens) and side-view images of our contact lens with four CSCM concentric arcs. Each CSCM is around 8.2 μm in radius (Fig. 5*D*). The pattern shows iridescent colors attributed to the angle dependence of the CSCM color as the substrate of the contact lens surface is curved (40). Due to the Janus property of the microdome color (40), a colorful pattern is visible from the convex side of the contact lens (Fig. 5 *C*, *Inset*), while it is transparent from the concave side (*SI Appendix*, Fig. S38). Thus, the pattern will not blur vision. We illuminated it with four-segmented polarized light (0°, 45°, 90°, and 135°, respectively) and captured the images using a digital camera. We obtained four polarimetric images filtered by different polarized analyzers (0°-LP, 90-°LP, LHC, and RHC, respectively) and a standard image without polarization analyzer (Fig. 5*E*). These images agree well with the target graphics. Therefore, our proposed contact lenses with CSCMs can offer comprehensive, multitiered security for personal identification.

The successful integration of CSCMs into contact lenses opens avenues for advancing information security in identity authentication and potentially enhancing human–computer interaction through the incorporation of diverse optical components. While these results are promising for high-dimensional information security, there are still some aspects that can be improved, particularly with regard to the surface texture of the contact lens. For instance,

Downloaded from https://www.pnas.org by FUDAN UNIVERSITY on February 25, 2025 from IP address 202.120.234.33.

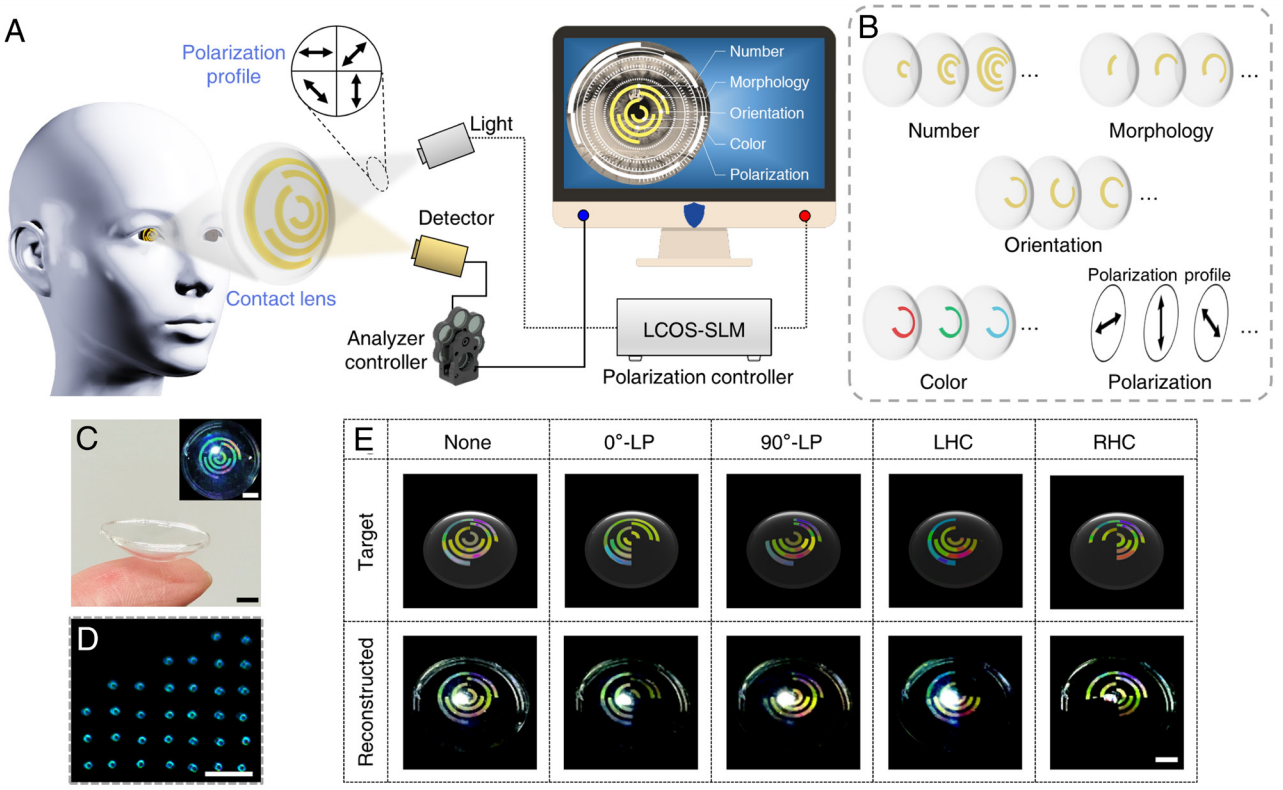

Fig. 5. Contact lenses integrated with CSCMs for identity authentication. (*A*) Conceptual illustration of identity authentication. (*B*) Schematic of the coding capability of the CSCM concentric arc pattern. (*C*) Optical images of the contact lens with CSCMs. (Scale bar, 3 mm.) (*D*) Dark-field optical micrographs of the inverted CSCM pixels. (Scale bar, 100 μm.) (*E*) The comparison between the designed graphics and experimental captured images. Identity authentication can only be passed when all images match. (Scale bar, 3 mm.)

the CSCMs fabricated on the inner surface of the contact lens could cause eye irritation due to the microscale bumps. Fortunately, this concern can be addressed by applying a smooth coating to encapsulate the CSCMs (44), ensuring the necessary smoothness on the inner surface to prevent irritation during direct contact with the eye.

Additionally, although polarizers reduce the total intensity of light reaching the viewer, the light loss varies significantly between different polarization analyzers, creating a strong contrast between orthogonal polarizers. This contrast is crucial for creating high-contrast images between the LHC and RHC polarizers, which can be exploited to encode information in our system, making it a valuable tool for applications such as optical encryption (A detailed discussion of these results can be found in *SI Appendix, Supplementary Text*).

Conclusions

In summary, we have found and verified the chiral structural color of CSCMs. These CSCMs with precise dimensions are easily made by printing with a common transparent polymer ink. The synergy of TIR and interference induces the structural colors of the CSCMs under light irradiation. Meanwhile, a $\pi/2$ phase delay of two orthogonal components of LP incidence occurs through multiple TIRs, leading to the chiroptics of CSCMs. The color and pattern of CSCMs can be well controlled by droplet-by-droplet printing using an ordinary inkjet printer and transparent polymer ink. Thus, the CSCMs, as optical codes, present multiple degrees of freedom including color, polarization, and pattern, bringing the merits of expanded storage capacity and improved information security. The CSCMs provide wide application potential in display, information storage, and data security. We have leveraged these CSCMs to realize full-color imaging and multichannel information encryption. Moreover, the CSCMs are easily compatible with wearable devices. We constructed contact lenses with CSCM code for identity authentication, similar to the iris recognition.

Methods

Materials and Chemicals.

Materials. Quartz glasses (dimension: 24 mm (L) × 24 mm (W) × 0.15 mm (H), 50 mm (L) × 50 mm (W) × 0.5 mm (H), Nanjing Upu Technology Co., Ltd., China); ***Chemicals.*** All chemicals were used as received. Sylgard 184 PDMS was purchased from Dow Corning Corporation Ltd. 1H,1H,2H,2H-perfluorodecyltrimethoxysilane (PFOTS) was purchased from Sigma-Aldrich. The polymer ink (InkOrmo, Micro Resist Technology, Germany) with the refractive index of 1.54 was purchased from Suzhou Yancai Micro and Nano Technology Co. Ltd. Polystyrene (PS) and polymethyl methacrylate (PMMA) microspheres (~10 μm in diameter) were purchased from Huge Biotechnology Corporation Ltd. PMMA powder was purchased from Beijing Innochem Science & Technology Co., Ltd. N, N-dimethyl acetamide (DMAc) was purchased from Beijing Innochem Science & Technology Co., Ltd.

Fabrication of CSCMs.

Fabrication of the transparent and hydrophobic substrates. The substrate was prepared by spin-coating (2,000 rpm, 30 s) the PDMS prepolymer (the precursor: the curing agent = 10:1 in weight ratio) on a quartz glass, followed by curing at 70 °C in an oven for 2 h. To increase the surface energy, the transparent PDMS-coating quartz glass was treated with air plasma (DT-02S, OPS Plasma Technology Co. Ltd., China) at 150 W for 200 s. Then, the surface of PDMS became sufficiently hydrophilic. After surface modified with PFOTS by chemical vapor deposition at 110 °C for 4 h, the transparent PDMS-coating quartz glass with low surface energy was fabricated.

The quartz glass was sequentially washed with detergent, deionized water, acetone, and isopropanol and then blow-dried with nitrogen. The PDMS prepolymer was mixed with its curing agent at a mass ratio of 10:1 and stirred by a mechanical stirrer for 5 min.

Inkjet printing. We used an inkjet printing system (DMP-2831, Dimatix Fujifilm, Japan) to prepare the chiral microdome structural color materials (CSCMs) by

Downloaded from https://www.pnas.org by FUDAN UNIVERSITY on February 25, 2025 from IP address 202.120.234.33.

printing the polymer ink on the hydrophobic substrate. The dimension of the CSCMs were well controlled by adjusting the ink's volume.

Design and Fabrication of the Patterned Polarizers.

Design of the sketch pattern for the patterned polarization mask used in brightness imaging. The sketch pattern was created by transforming a geometric object photograph into a grayscale image using image processing software. The gray level of each pixel in the grayscale image corresponds to the designed incidence polarization angle for each microdome. The grayscale image was then imported into the computer to fabricate the patterned polarization mask.

Design of the pattern in the patterned linear polarizer used for multichannel information storage. First, the rabbit pattern is encoded onto the polarization profile with a polarization angle of 45°, and the associated pixels are marked in orange. The duck pattern is encoded onto the polarization profile with a polarization angle of 135°, and the associated pixels are designated in green. The overlapping pixels, marked in red, are encoded onto the polarization profile with a polarization angle of 0° as the overlapped pixels can be seen in both LCP and RCP channels. Then, the image was divided into three subgraphs based on its color channels (orange, green, and red). Finally, these subgraphs were converted into grayscale images, and their gray levels were adjusted using image processing software. These grayscale images were used for fabricating the patterned linear polarizer.

Design of the encrypted pattern in the patterned linear polarizer used for multichannel information encryption. First, the Mo Zi portrait was encoded in the LCP channel with the associated pixels marked in orange while the Fresnel portrait was encoded in the RCP channel with the associated pixels designated in green (*SI Appendix*, Fig. S35 *A* and *B*). Second, their overlapping pixels, encoded simultaneously in both channels, were marked in yellow (*SI Appendix*, Fig. S35*C*). As the overlapped pixels can pass through both LCP and RCP channels with the same intensity, their polarization states are LP. Thus, three different polarization angles (45°, 90°, and 135°) were used to generate LCP, LP, and RCP light, respectively, at a specific viewing angle. Third, the image was divided into three subgraphs based on its color channels (orange, green, and yellow). Finally, these subgraphs were converted into grayscale images and adjusted their gray level using image processing software. These grayscale images were used for fabricating the patterned linear polarizer.

Design of the four-segmented circle pattern in the patterned linear polarizer used for identity authentication. The four-segmented circle pattern was drawn using software (Microsoft Paint), with each segment filled with a different grayscale color. Then, the four-segmented circle pattern was then imported into the computer to fabricate the patterned linear polarizer.

Fabrication of the patterned linear polarizer (the patterned polarization mask). First, electrodes and alignment layers are fabricated on a transparent substrate to precisely control the orientation of the liquid crystal molecules. Here, laser direct writing technology is used to pattern the electrodes and alignment layers based on the input grayscale image, and create multiple regions on the same liquid crystal polymer layer, with each region having a different molecular alignment. Second, different layers of liquid crystal polymers are sequentially deposited using spin-coating or other techniques. The refractive index and thickness of each layer are precisely designed so that each region produces the same phase retardation at different wavelengths, achieving achromatic performance across a wide wavelength range. Third, laser direct-write technology is employed to adjust the molecular orientation of each liquid crystal polymer layer to optimize phase modulation. Finally, the alignment of the liquid crystal molecules is fixed through photopolymerization or thermal curing, and the half-wave plate is encapsulated to ensure long-term stability and optical performance.

Characterizations.

CA measurement of the CSCM. The CAs of CSCM were measured using contact angle measurement equipment (OCA20, Data Physics, Germany).

SEM characterization of the CSCMs. The microstructures of CSCMs were tested by a field-emission SEM (JEOL, JSM-7500F, Japan) at an accelerating voltage of 5.0 kV. For the cross-sectional observation, the CSCMs were fractured when submerged in the liquid nitrogen. All the samples were coated with platinum.

Optical microscopy and imaging. The optical micrographs of CSCMs were recorded by an optical microscope (Nikon ECLIPSE Ti) equipped with a halogen illuminator (Nikon LV-LH50PC) in reflection mode. The numerical aperture (NA) of the objective lens for optical microscopy used in our experiment is 0.15. The optical morphology of the CSCMs was characterized by using a bright-field reflection microscope. The color of the inverted CSCMs was characterized by using a dark-field reflection microscope set-up illuminated by a white light source. The dark-field reflective mode imaging was performed under illumination with an angle of 8.6°.

Reflectance spectra. The reflectance spectra of CSCMs were measured by an angle-resolved spectrum system (R1, Ideaoptics, China) equipped with a high-sensitive spectrometer (NOVA, Ideaoptics, China). The CSCM sample was put on a stage in the center of the measurement system and illuminated with a collimated incident beam on the surface. Measurements were recorded at a fixed incident light angle (8°, defined from the normal of the sample interface), and collected spectral intensity at the retroreflection angles (0°).

Optical photography. The optical images were captured using a smartphone Apple iPhone 13 Pro. For large area illumination, a Godox LED 50 W light with a collimating lens was used to illuminate the sample.

Polarized photography. The CSCMs were illuminated from the back (glass side) by polarized white light, and the scattered light was captured using a smartphone Apple iPhone 13 Pro. To create linear polarization light, the white light passed through a linear polarizer. To obtain the polarized images, the light scattered by the CSCMs passed through a quarter-wave plate and an orientable linear polarizer, which together can filter either LCP or RCP light scattered by the sample.

CD spectra. Chiroptical responses of CSCMs were characterized with a commercial circular dichroic spectrometer (J-1700, JASCO Corporation, Japan) equipped with an integrating sphere for solid-state samples. The scan parameters were as follows: scanning speed = 500 nm/min, data pitch = 0.5 nm, and wavelength range = 250 to 800 nm.

Data, Materials, and Software Availability. The MATLAB code used to implement the model is available for download from OSF (https://osf.io/zj58v/?view_only=2a3aeb13e33d497baa8aac925ff1a97b) (43). All other data are included in the manuscript and/or *SI Appendix*.

ACKNOWLEDGMENTS. This work was financially supported by the National Science Fund for Distinguished Young Scholars (22225502), the National Natural Science Foundation of China (22073107, 52321006, and 2150410331), the National Key R&D Program of China (2022YFE0202000 and 2018YFA0208500), and Bureau of International Cooperation, Chinese Academy of Sciences (027GJHZ2022044MI). We thank Dr. K.X. Li for technical assistance with the inkjet printer. We are grateful to Y.Y. Zhuang for assistance with grayscale image designing. We are grateful to M.H. Liu for discussion about the mechanism of chiral structural color.

Author affiliations: [a]Key Laboratory of Bio-Inspired Materials and Interface Science, Technical Institute of Physics and Chemistry, Chinese Academy of Sciences, Beijing 100190, People's Republic of China; [b]Key Laboratory of Green Printing, Institute of Chemistry, Chinese Academy of Sciences, Beijing 100190, People's Republic of China; [c]State Key Laboratory of Surface Physics, Key Laboratory of Micro- and Nano-Photonic Structures (Ministry of Education) and Department of Physics, Fudan University, Shanghai 200433, People's Republic of China; [d]Department of Engineering Physics, Münster University of Applied Sciences, Steinfurt 48565, Germany; [e]Collaborative Innovation Center of Advanced Microstructures, Nanjing University, Nanjing 210008, People's Republic of China; and [f]School of Future Technology, University of Chinese Academy of Sciences, Beijing 100190, People's Republic of China

1. H. Wang *et al.*, Full color and grayscale painting with 3D printed low-index nanopillars. *Nano Lett.* **21**, 4721–4729 (2021).
2. J. Y. E. Chan *et al.*, High-resolution light field prints by nanoscale 3D printing. *Nat. Commun.* **12**, 3728 (2021).
3. H. T. Wang *et al.*, Optical fireworks based on multifocal three-dimensional color prints. *ACS Nano* **15**, 10185–10193 (2021).
4. S. U. Kim *et al.*, Broadband and pixelated camouflage in inflating chiral nematic liquid crystalline elastomers. *Nat. Mater.* **21**, 41–46 (2022).
5. M. Song *et al.*, Versatile full-colour nanopainting enabled by a pixelated plasmonic metasurface. *Nat. Nanotechnol.* **18**, 71–78 (2023).
6. B. H. Miller, H. Liu, M. Kolle, Scalable optical manufacture of dynamic structural colour in stretchable materials. *Nat. Mater.* **21**, 1014–1018 (2022).

Downloaded from https://www.pnas.org by FUDAN UNIVERSITY on February 25, 2025 from IP address 202.120.234.33.

7. A. L. Holsteen, A. F. Cihan, M. L. Brongersma, Temporal color mixing and dynamic beam shaping with silicon metasurfaces. *Science* **365**, 257–260 (2019).
8. K. L. Liu *et al.*, 3D printing colloidal crystal microstructures via sacrificial-scaffold-mediated two-photon lithography. *Nat. Commun.* **13**, 4563 (2022).
9. F. Bian *et al.*, Bioinspired MXene-integrated colloidal crystal arrays for multichannel bioinformation coding. *Proc. Natl. Acad. Sci. U.S.A.* **117**, 22736–22742 (2020).
10. Q. Chen *et al.*, All-inorganic perovskite nanocrystal scintillators. *Nature* **561**, 88–93 (2018).
11. P. P. Muhoray, Liquid crystals new designs in cholesteric colour. *Nature* **391**, 745–746 (1998).
12. S. Jahani, Z. Jaco, All-dielectric metamaterials. *Nat. Nanotechnol.* **11**, 23–36 (2016).
13. P. Chen *et al.*, Liquid-crystal-mediated geometric phase: From transmissive to broadband reflective planar optics. *Adv. Mater.* **32**, e1903665 (2020).
14. Y. Chang *et al.*, Cell wall composition determines handedness reversal in helicoidal cellulose architectures of *Pollia condensata* fruits. *Proc. Natl. Acad. Sci. U.S.A.* **118**, e2111723118 (2021).
15. N. H. Cho *et al.*, Bioinspired chiral inorganic nanomaterials. *Nat. Rev. Bioeng.* **1**, 88–106 (2023).
16. B. Frka-Petesic *et al.*, Structural color from cellulose nanocrystals or chitin nanocrystals: Self-assembly, optics, and applications. *Chem. Rev.* **123**, 12595–12756 (2023).
17. V. Sharma *et al.*, Structural origin of circularly polarized iridescence in jeweled beetles. *Science* **325**, 449–451 (2009).
18. S. Vignolini *et al.*, Pointillist structural color in Pollia fruit. *Proc. Natl. Acad. Sci. U.S.A.* **109**, 15712–15715 (2012).
19. T. H. Chiou *et al.*, Circular polarization vision in a stomatopod crustacean. *Curr. Biol.* **18**, 429–434 (2008).
20. P. Vukusic, Evolutionary photonics with a twist. *Science* **325**, 398–399 (2009).
21. L. Wang, A. M. Urbas, Q. Li, Nature-inspired emerging chiral liquid crystal nanostructures: From molecular self-assembly to DNA mesophase and nanocolloids. *Adv. Mater.* **32**, 1801335 (2020).
22. Z. W. Li *et al.*, A magnetic assembly approach to chiral superstructures. *Science* **380**, 1384–1390 (2023).
23. R. M. Kim *et al.*, Enantioselective sensing by collective circular dichroism. *Nature* **612**, 470–476 (2022).
24. P. Chen *et al.*, Chirality invertible superstructure mediated active planar optics. *Nat. Commun.* **10**, 2518 (2019).
25. Z. G. Zheng *et al.*, Digital photoprogramming of liquid-crystal superstructures featuring intrinsic chiral photoswitches. *Nat. Photonics.* **16**, 226–234 (2022).
26. Z. G. Zheng *et al.*, Three-dimensional control of the helical axis of a chiral nematic liquid crystal by light. *Nature* **531**, 352–356 (2016).
27. K. Hou *et al.*, Optically active inverse opal photonic crystals. *J. Am. Chem. Soc.* **140**, 16446–16449 (2018).
28. J. W. Lv *et al.*, Biomimetic chiral photonic crystals. *Angew. Chem. Int. Ed. Engl.* **58**, 7783–7787 (2019).
29. J. Lu *et al.*, Enhanced optical asymmetry in supramolecular chiroplasmonic assemblies with long-range order. *Science* **371**, 1368–1374 (2021).
30. B. E. Droguet *et al.*, Large-scale fabrication of structurally coloured cellulose nanocrystal films and effect pigments. *Nat. Mater.* **21**, 352–358 (2022).
31. B. Frka-Petesic, S. Vignolini, Cellulose, so much more than paper. *Nat. Photonics* **13**, 365–367 (2019).
32. H. E. Lee *et al.*, Amino-acid- and peptide-directed synthesis of chiral plasmonic gold nanoparticles. *Nature* **556**, 360–365 (2018).
33. Z. S. Gan, M. D. Turner, M. Gu, Biomimetic gyroid nanostructures exceeding their natural origins. *Sci. Adv.* **2**, e1600084 (2016).
34. P. T. Probst *et al.*, Mechano-tunable chiral metasurfaces via colloidal assembly. *Nat. Mater.* **20**, 1024–1028 (2021).
35. X. F. Zhang *et al.*, Uniformly aligned flexible magnetic films from bacterial nanocelluloses for fast actuating optical materials. *Nat. Commun.* **13**, 5804 (2022).
36. X. Zhang *et al.*, Liquid crystal-templated chiral nanomaterials: From chiral plasmonics to circularly polarized luminescence. *Light Sci. Appl.* **11**, 223 (2022).
37. K. E. Shopsowitz *et al.*, Free-standing mesoporous silica films with tunable chiral nematic structures. *Nature* **468**, 422–425 (2010).
38. M. J. Zhang *et al.*, Processable circularly polarized luminescence material enables flexible stereoscopic 3D imaging. *Sci. Adv.* **9**, eadi9944 (2023).
39. A. E. Goodling *et al.*, Colouration by total internal reflection and interference at microscale concave interfaces. *Nature* **566**, 523–527 (2019).
40. K. X. Li *et al.*, Facile full-color printing with a single transparent ink. *Sci. Adv.* **7**, eabh1992 (2021).
41. A. M. Szalai *et al.*, Three-dimensional total-internal reflection fluorescence nanoscopy with nanometric axial resolution by photometric localization of single molecules. *Nat. Commun.* **12**, 517 (2021).
42. D. H. Goldstein, *Polarized Light* (CRC Press, ed. 3, 2017), pp. 1–770.
43. X. T. Lai *et al.*, Chiral structural color from microdomes. Open Science Framework. https://osf.io/zj58v/?view_only=2a3aeb13e33d497baa8aac925ff1a97b. Deposited 25 December 2024.
44. N. E. K. Sturniolo *et al.*, Iridescence from total internal reflection at 3D microscale interfaces: Mechanistic insights and spectral analysis. *Adv. Mater.* **35**, 2210665 (2023).

Downloaded from https://www.pnas.org by FUDAN UNIVERSITY on February 25, 2025 from IP address 202.120.234.33.